Supplementary Information

Triboelectric tactile sensor for pressure and temperature sensing in high-temperature applications

*Yanhua Liu[1], Jinlong Wang[1], Tao Liu[1], Zhiting Wei[1], Bin Luo[1], Mingchao Chi[1], Song Zhang[1], Chenchen Cai[1], Cong Gao[1], Tong Zhao[1], Shuangfei Wang[1], Shuangxi Nie[1,] **

[1]Guangxi Key Laboratory of Clean Pulp & Papermaking and Pollution Control, School of Light Industry and Food Engineering, Guangxi University, Nanning 530004, PR China

*Corresponding author. Email: nieshuangxi@gxu.edu.cn (S. Nie)

This PDF file includes:

- Supplementary Text
- Supplementary Figures 1-16
- Supplementary Tables 1-2
- Supplementary References

Other Supplementary Materials for this manuscript include the following:

- Supplementary Movies 1-3

Supplementary Text

Supplementary Note 1 | Principle of triboelectric signal generation.

According to the working principle of TENG, when two triboelectric layers come into contact, due to the contact electrification effect, the inner surfaces of the two layers acquire opposing static charges (tribo-charges Q) with equal density of σ. As the two layers begin to separate and distance (x) increases, a potential difference (V) is induced between the electrodes. Niu et al.[1] studied the fundamental equations for contact-mode TENG, which can be used to calculate its output characteristics:

$$V = -\frac{Q}{S\varepsilon_0}\left(d_0 + x(t)\right) + \frac{\sigma x(t)}{\varepsilon_0} \tag{1}$$

Under open-circuit conditions, no charge is transferred, which means Q is 0. Thus, the open-circuit voltage (V_{OC}) can be expressed with the following Equation:

$$V_{\mathrm{OC}} = \frac{\sigma x(t)}{\varepsilon_0} \tag{2}$$

Where σ is the triboelectric charge density, ε_0 is the vacuum permittivity, and $x(t)$ is the gap between the two contact materials. From Equation (2), it is evident that during this process, the open-circuit voltage is independent of frequency and only increases with the rise in displacement. When the displacement (x) reaches x_{max}, the maximum open-circuit voltage is achieved[2].

Supplementary Note 2 | Theoretical analysis of pressure and voltage sensing signal.

Usually, under pressure (P), the output voltage (U_{p}) of a TENG equals the open-circuit voltage (V_{OC}) in that state, which can be expressed by the formula[3]:

$$U_{\mathrm{p}} = \frac{\sigma_0 d_{\mathrm{p}}}{\varepsilon_0} \tag{3}$$

Where ε_0 is the vacuum permittivity constant, and σ_0 is the triboelectric charge density, considered constant. Assume the initial gap distance is d_0 with a change Δd, and d_{p} is the distance under P. The gap distance and open-circuit voltage under P can be calculated as follows:

$$d_{\mathrm{p}} = d_0 - \frac{d_0}{Y}P \tag{4}$$

$$U_{\mathrm{p}} = \frac{\sigma_0}{\varepsilon_0}\left(d_0 - \frac{d_0}{Y}P\right) \quad (5)$$

Where Young's modulus (Y), the initial distance of the gap layer (d_0), triboelectric charge density (σ_0), and permittivity constant (ε_0) can be considered constants. The open-circuit voltage (U_{p}) is expected to have a direct linear relationship with the external P, making it a reliable parameter for measuring the pressure applied to the sensor. Different voltage increases lead to different sensitivities. Hence, the larger the voltage signal, the higher the sensitivity[4, 5].

Supplementary Note 3 | Analysis of sensing principle for T-TENG.

According to the thermionic emission effect (Equation 6)[6] and extended the law of surface charge index decay at high temperature (Equation 7), Lin et.al[7] further introduced the σ_{p} term to describe the thermionic emission model (Equation 8),

$$J = \lambda A_0 T^2 \mathrm{e}^{\frac{W}{kT}}\left[\mathrm{e}^{\frac{\Delta w}{kT}} - 1\right] \quad (6)$$

$$\sigma = \mathrm{e}^{-at}\sigma_{\mathrm{i}} \quad (7)$$

$$\sigma = \mathrm{e}^{-at}\sigma_{\mathrm{e}} + \sigma_{\mathrm{p}} \quad (8)$$

Where J is the thermionic emission current density, λ is the material-specific correction factor, A_0 is the Richardson constant of free electrons, T is the temperature, W is the height of the potential barrier, k is the Boltzmann constant, ΔW is the change in the height of the potential barrier caused by the surface electric field, σ is the surface charge density, a is the decay coefficient, σ_{i} is the initial charge density, t is the dissipation time, σ_{e} is the triboelectric charge, σ_{p} is the “permanent” charge retained on the surface.

Supplementary Note 4 | The feature matrix of stimulation and response electrical signals of the multimodal triboelectric sensor.

The simultaneous occurrence of n stimuli, denoted as 's', induces changes in m electrical parameters, denoted as 'p'. The relationship between p and s can be represented as follows.

$$p = f(s) = \begin{bmatrix} p_1 \\ p_2 \\ \cdots \\ p_n \end{bmatrix} = \begin{bmatrix} f_1(s_1, s_2, \ldots s_n) \\ f_2(s_1, s_2, \ldots s_n) \\ \vdots \\ f_m(s_1, s_2, \ldots s_n) \end{bmatrix} \tag{9}$$

The Jacobian matrix is defined as

$$J(s) = \begin{bmatrix} \frac{\partial f_1}{\partial s_1} & \frac{\partial f_1}{\partial s_2} & \cdots & \frac{\partial f_1}{\partial s_n} \\ \frac{\partial f_2}{\partial s_1} & \frac{\partial f_2}{\partial s_2} & \cdots & \frac{\partial f_2}{\partial s_n} \\ & & \vdots & \\ \frac{\partial f_m}{\partial s_1} & \frac{\partial f_m}{\partial s_2} & \cdots & \frac{\partial f_m}{\partial s_n} \end{bmatrix} \tag{10}$$

At s = s_0, and small Δs, we have the following relationship

$$\begin{bmatrix} \Delta p_1 \\ \Delta p_2 \\ \vdots \\ \Delta p_n \end{bmatrix} = \begin{bmatrix} \frac{\partial f_1}{\partial s_1} & \frac{\partial f_1}{\partial s_2} & \cdots & \frac{\partial f_1}{\partial s_n} \\ \frac{\partial f_2}{\partial s_1} & \frac{\partial f_2}{\partial s_2} & \cdots & \frac{\partial f_2}{\partial s_n} \\ & & \vdots & \\ \frac{\partial f_m}{\partial s_1} & \frac{\partial f_m}{\partial s_2} & \cdots & \frac{\partial f_m}{\partial s_n} \end{bmatrix}_{s=s0} \begin{bmatrix} \Delta s_1 \\ \Delta s_2 \\ \vdots \\ \Delta s_n \end{bmatrix} \text{ or } \Delta p_1 = J(s)\Delta s \tag{11}$$

The Jacobian matrix M can be derived from the theoretical expression of p and s or experimental data.

$$\begin{bmatrix} \Delta T \\ \Delta P \end{bmatrix} = \begin{bmatrix} M_1 & M_2 \\ M_3 & M_4 \end{bmatrix} \begin{bmatrix} \Delta U_{\mathrm{T}} \\ \Delta U_{\mathrm{P}} \end{bmatrix} \tag{12}$$

Where ΔU_{T} and ΔU_{P} are the changes in U_{T} and U_{P} under the stimulus of temperature (T, ΔT) and pressure (P, ΔP). M_1, M_2, M_3 and M_4 are the subcomponents of the matrix M.

Supplementary Figures

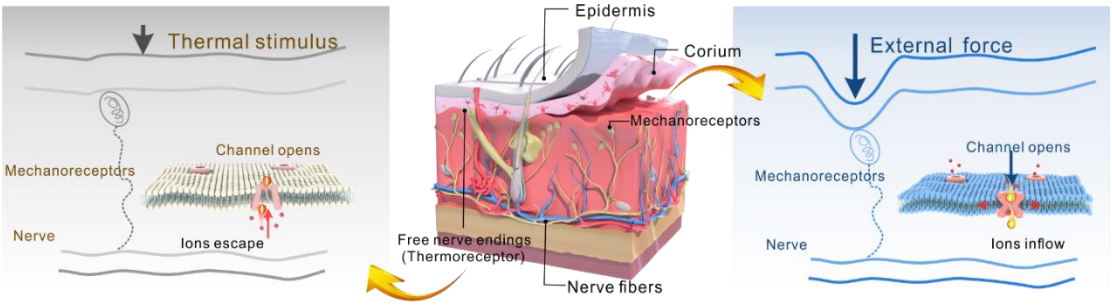

Supplementary Figure 1 | Schematic diagram of human skin mechanoreceptors and thermoreceptors and their sensing mechanisms.

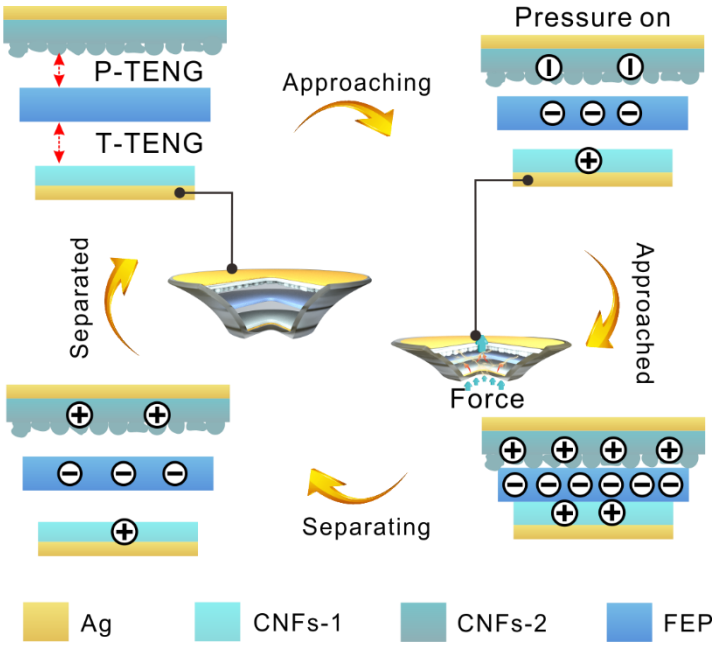

Supplementary Figure 2 | Schematic diagram of the working mode of the triboelectric sensor.

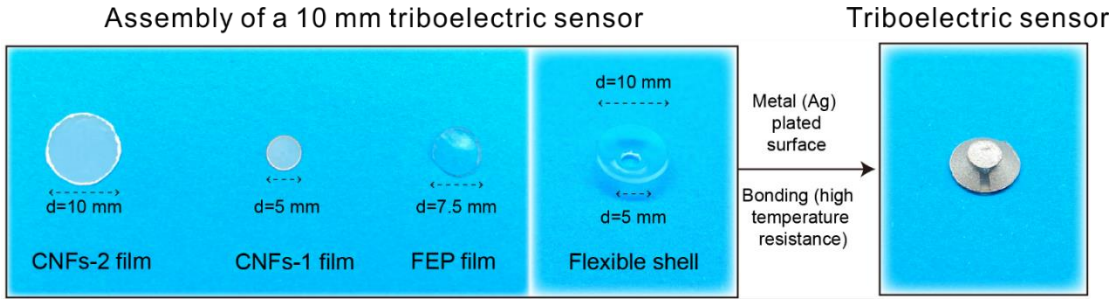

Supplementary Figure 3 | Optical images of the triboelectric sensor components and assembly process.

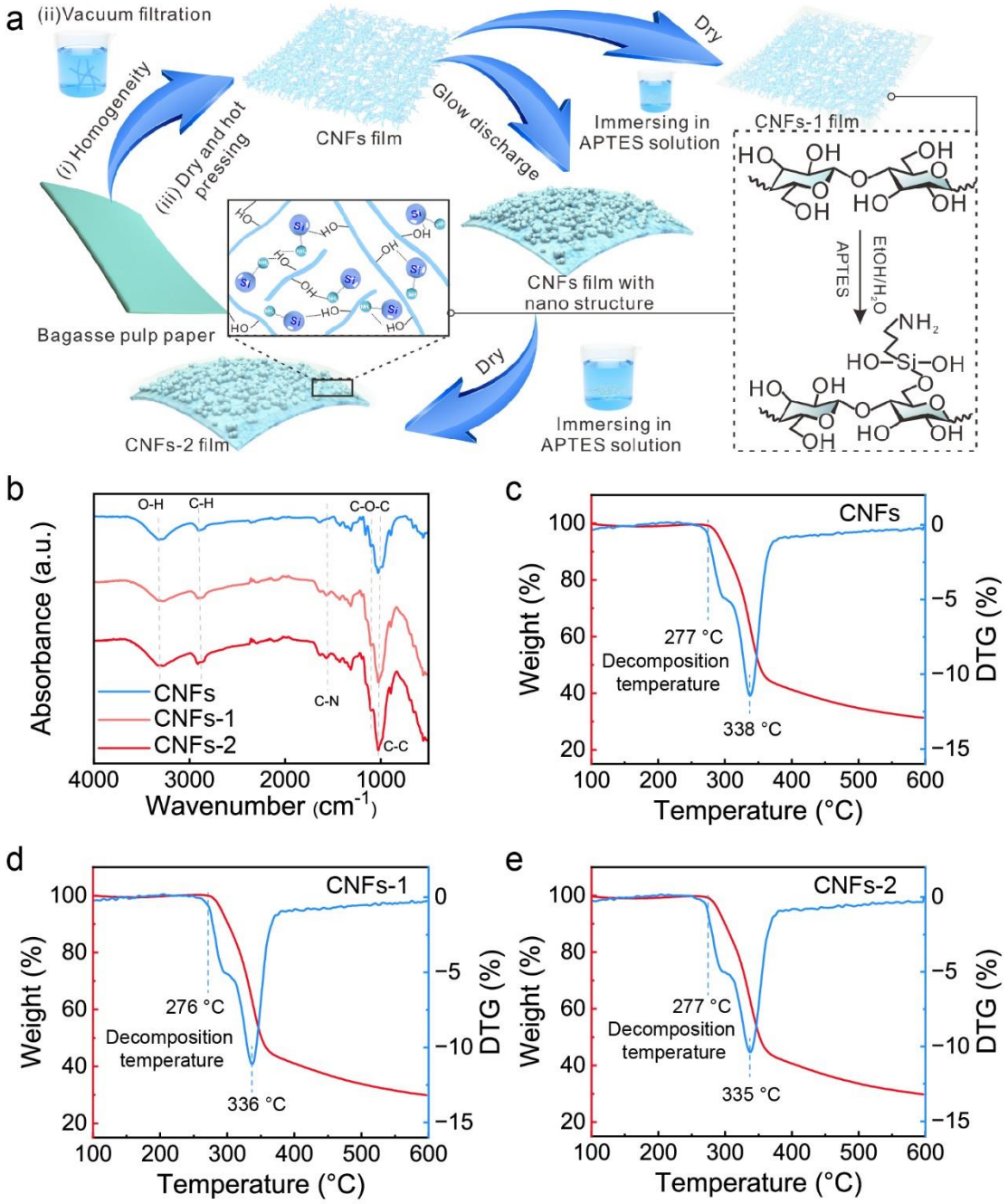

Supplementary Figure 4 | Preparation of samples. a Schematic diagram of the preparation process of CNFs film, CNFs-1 film and CNFs-2 film (illustrated chemical process). **b** Fourier transform infrared spectral images of CNFs film, CNFs-1 film and CNFs-2 film. **c-e** Thermogravimetric analysis images of CNFs films, CNFs-1 film and CNFs-2 film, respectively.

The fabrication schematic illustration of the temperature-sensing material (CNFs-1) and pressure-sensing material (CNFs-2) of T-TENG and P-TENG is shown in Supplementary Fig. 4 (See the Methods section for specific details).

Fourier Transform Infrared (FTIR) spectroscopy was employed to characterize the chemical groups in the samples. Compared to the pristine CNFs film, both CNFs-1 films and CNFs-2 films exhibited distinct characteristic peaks at 781 cm^{-1} and 1573 cm^{-1}, respectively, corresponding to -Si-O-C and -NH_2 groups. This indicates the functionalization of CNFs with APTES, introducing amine groups with enhanced triboelectric properties into the CNFs film.

The thermal stability of the triboelectric materials was assessed using thermogravimetric analysis (TG). The initial decomposition temperatures of all three fiber-based materials were above 275 °C, with maximum decomposition temperatures around 366 °C. Notably, the initial and maximum decomposition temperatures of CNFs-1 film and CNFs-2 film were nearly identical to those of pristine CNFs films. This suggests that the chemical modification treatment and low-temperature plasma technology did not alter the thermal stability of the fiber-based materials. The high thermal stability of CNFs-1 film and CNFs-2 film ensures the stable operation of the dual-mode sensors under elevated temperatures of up to 200 °C.

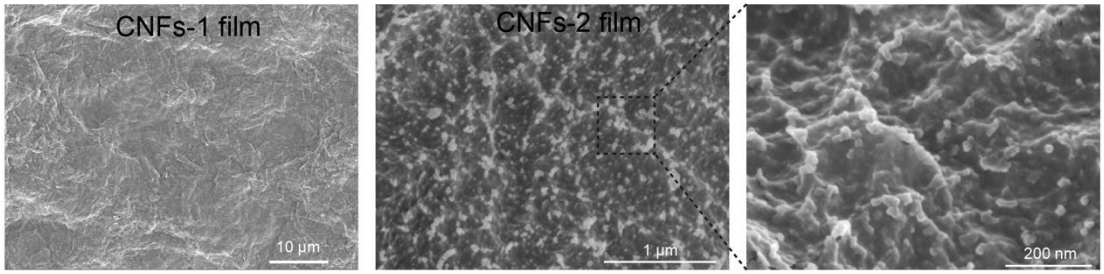

Supplementary Figure 5 | Scanning electron microscopy (SEM) images of CNFs-1 film without surface microstructure and CNFs-2 film with surface structure.

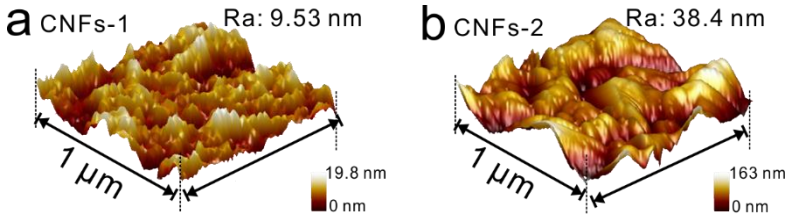

Supplementary Figure 6 | Atomic Force microscope (AFM) images of CNFs-1 film without surface microstructure and CNFs-2 film with surface structure, with surface roughness (RA) of 9.53 nm and 38.4 nm, respectively.

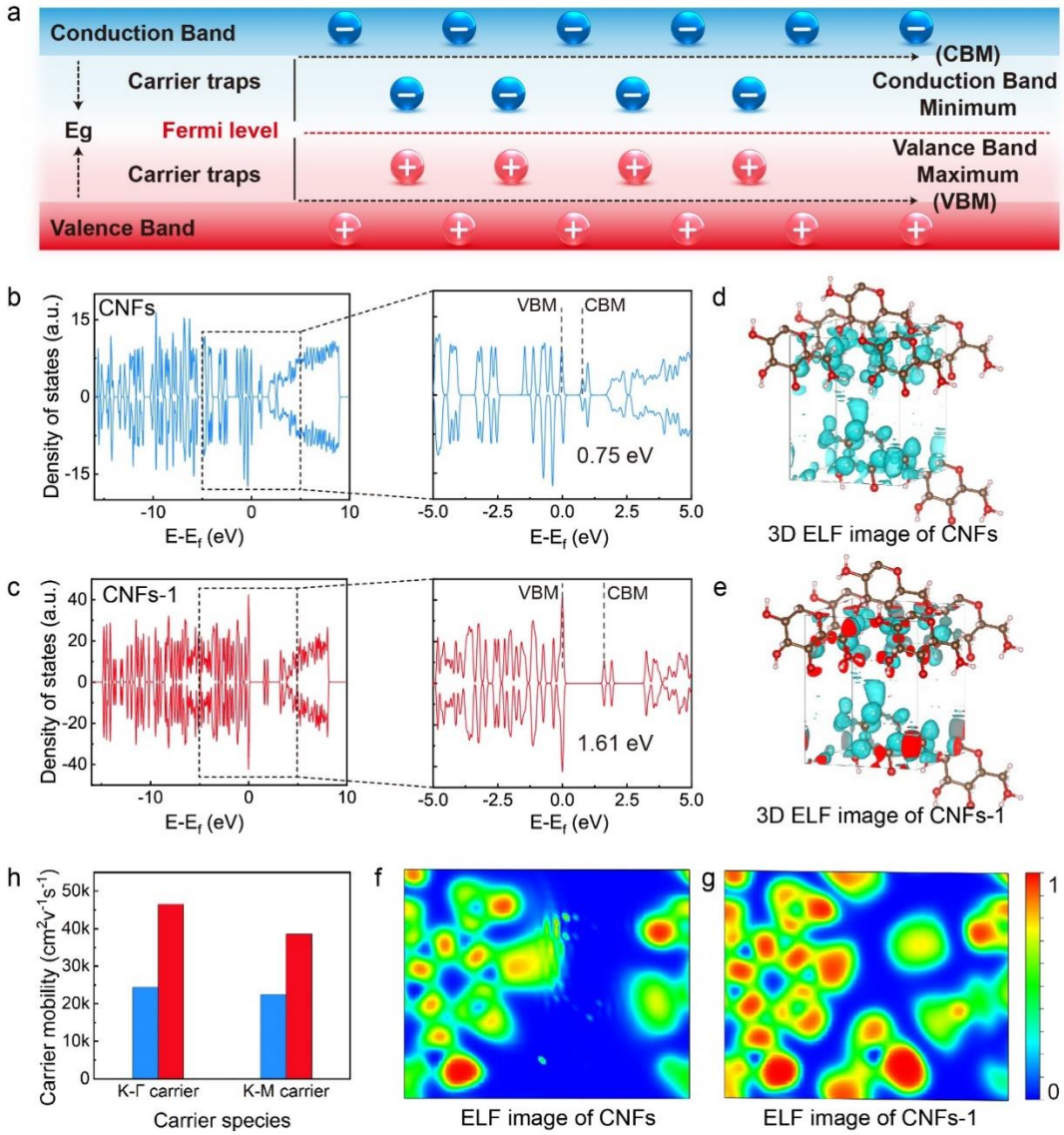

Supplementary Figure 7 | Characterization of samples. a Schematic diagram of the electronic band structure of cellulose triboelectric materials. **b, c** Density of States (DOS) of the molecular structure of CNFs and CNFs-1. **d, e** Electron Localization Function (ELF) 3D images of the molecular structure of CNFs and CNFs-1 with isosurface of 0.61 e/Å3 (charge accumulation shown as cyan region). **f, g** ELF of the molecular structure of CNFs and CNFs-1. **h** Carrier mobility of the molecular structure of CNFs and CNFs-1 (the carrier type is electron-hole).

Supplementary Fig. 7a presents a schematic diagram of the electronic band structure of cellulose triboelectric materials. The triboelectric charge generated by contact electrification is retained in the carrier traps of the band structure of the triboelectric material. The energy barrier and capture cross-section of the carrier traps confine the triboelectric charge to the electronic bandgap structure of the material.

Density functional theory (DFT) is used to analyze the density of states (DOS) of CNFs film. The result found that the bandgap of CNFs film is only 0.75 eV (Supplementary Fig. 7b, c), indicating that the carrier traps in the bandgap of CNFs film are closer to the band edges, requiring lower energy and resulting in weaker charge retention capability. The bandgap of the triboelectric material (CNFs-1) in the charge retention phase is as high as 1.61 eV. The carrier traps for triboelectric charge are located far from the conduction band minimum and valence band maximum, respectively, which can better retain triboelectric charge and improve the sensor response signal.

To further investigate the redistribution of electrons in the molecular structure, the electron localization function (ELF) was calculated and topological analysis was performed. Supplementary Fig. 7d, e show the three-dimensional ELF visualization maps with an isosurface value of 0.61 e/Å3, respectively. The blue regions in the figures represent the electron distribution areas. Compared with CNFs, CNFs-1 has more blue distributions, indicating more electron distributions. The two-dimensional quantitative ELF images (Supplementary Fig. 7f, g) also show that the molecular structure of CNFs-1 has more electrons around it. These results indicate that in the charge retention phase, triboelectric charges more easily to carrier traps, significantly improving triboelectric charge retention, which is more conducive to a higher sensor response signal in high-temperature environments.

To analyze the motion state of the charge in the sensing material, the carrier mobility is studied based on the variable situation theory proposed by Bardeen and Shockley, as shown in the equation:

$$\mu = \frac{\mathrm{e}h^3 C}{K_{\mathrm{B}} T m^* m_d \mathrm{E}_1^2} \tag{13}$$

Where e represents the elementary charge, $\hbar$ represents Planck's constant divided by 2π, K_{B} represents the Boltzmann constant, T represents the temperature set at 300 K. m^* denotes the effective mass of electrons or holes, and the carrier mobility can be derived from the derivative of the electronic band structure using the following formula, as illustrated in Supplementary Fig. 7h. The results reveal that the CNFs film molecular structure exhibits a high carrier mobility (24298 $cm^2V^{-1}s^{-1}$), indicating the rapid motion

of retained triboelectric charges within the band structure. Compared to CNFs, CNFs-1 exhibits further enhanced carrier mobility (46500 $cm^2V^{-1}s^{-1}$). DOS and ELF analyses demonstrate that CNFs-1 possesses a high triboelectric charge retention capability, leading to a more pronounced electrical response to stimuli. Additionally, CNFs-1 exhibits faster triboelectric charge motion. Under elevated temperatures, the rapidly moving triboelectric charges are susceptible to hot electron emission, resulting in a faster temperature change response for CNFs-1 in high-temperature environments.

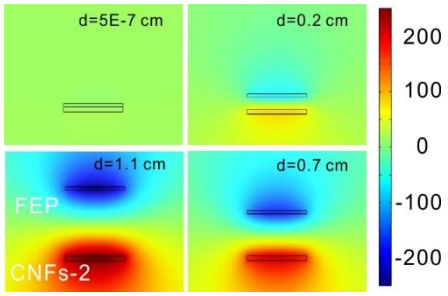

Supplementary Figure 8 | Finite element simulation of surface potential variation of triboelectric materials.

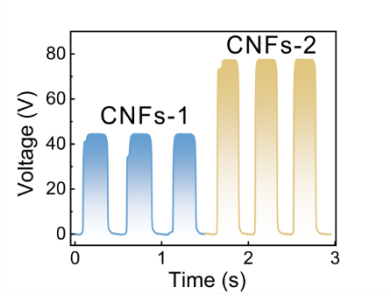

Supplementary Figure 9 | Comparison of output voltage of smooth and rough surface.

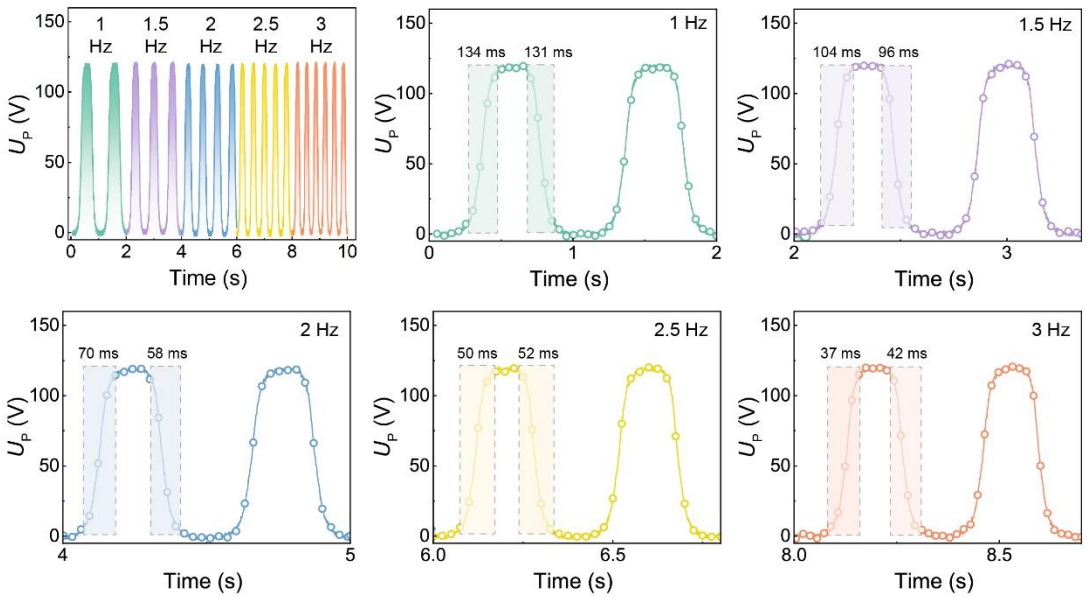

Supplementary Figure 10 | Electrical signal and response time of the pressure sensor at 1 Hz, 1.5 Hz, 2 Hz, 2.5 Hz and 3 Hz.

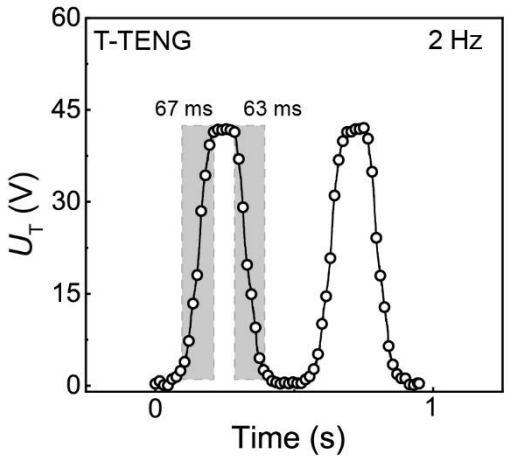

Supplementary Figure 11 | Response and recovery time of T-TENG.

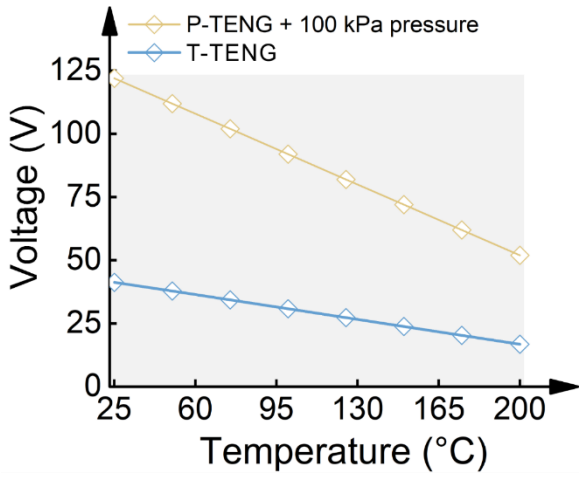

Supplementary Figure 12 | Theoretical data under ideal conditions. The cross-coupling error of P-TENG and T-TENG under different temperatures at 100 kPa is less than 0.4% and 3.2% respectively compared with the actual test signal.

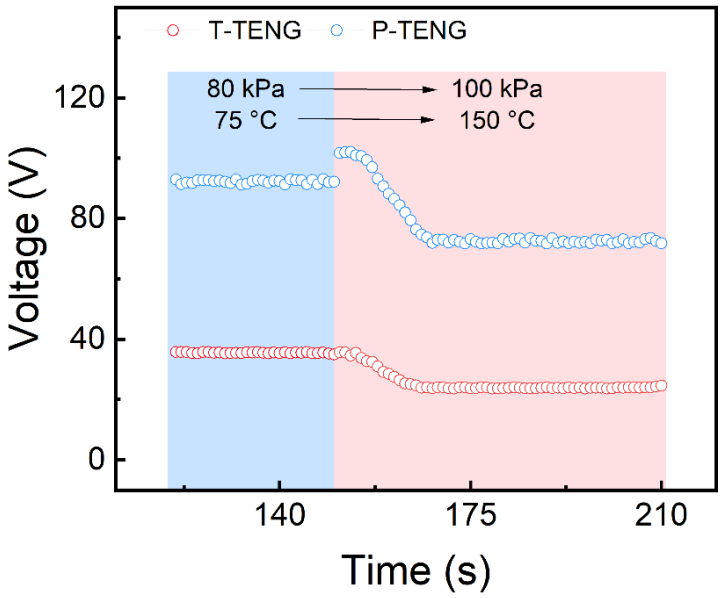

Supplementary Figure 13 | The electrical signal in which pressure and temperature change simultaneously.

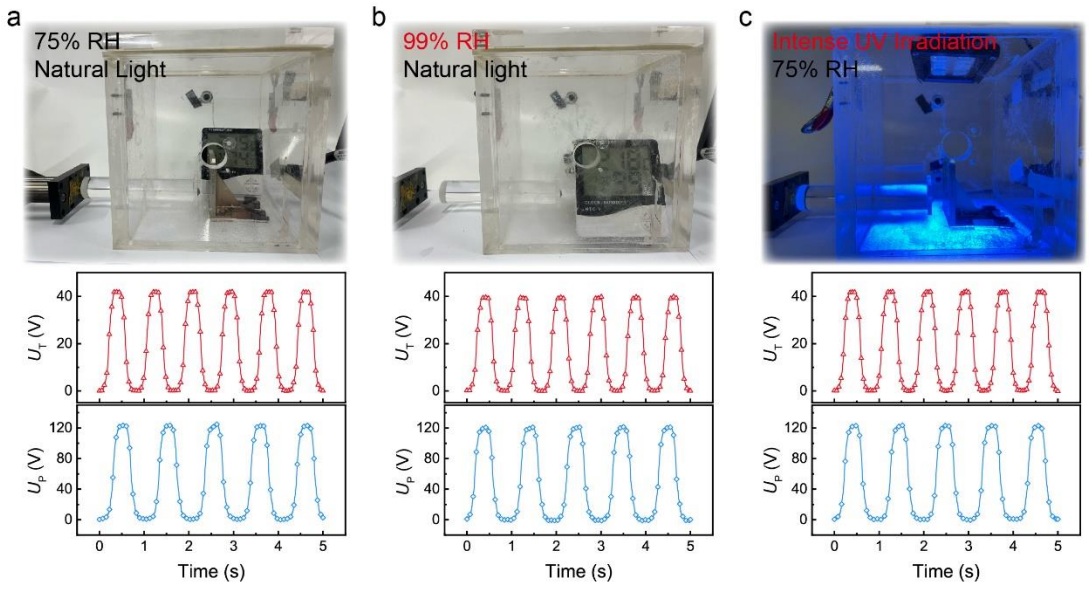

Supplementary Figure 14 | The electrical signals under humidity and ultraviolet light.

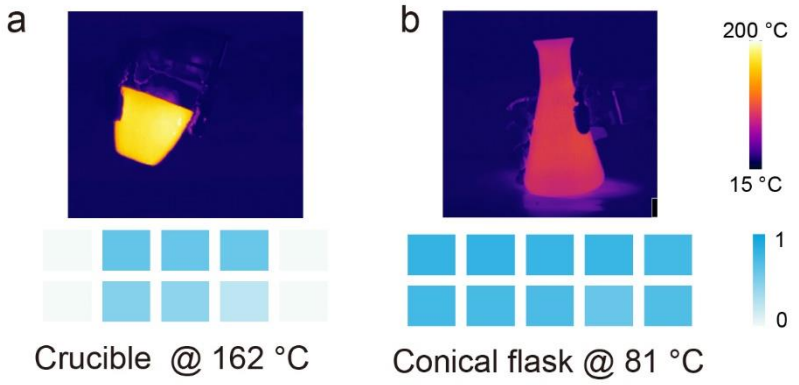

Supplementary Figure 15 | The recognition of asymmetric objects.

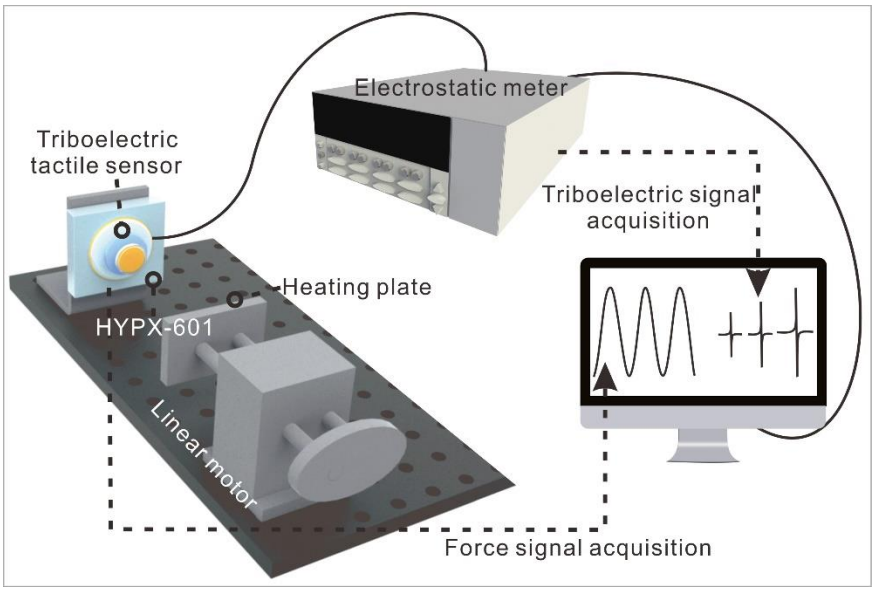

Supplementary Figure 16 | Diagram of the electrical performance testing device.

Supplementary Table 1 | Comparison of the temperature detection range of this work with reported multimodal sensors.

Multimodal sensing	Sensing mechanism	Temperature range (°C)	Reference
Pressure/temperature	Stress-optic/thermo-optic	26-35	[8]
Pressure/temperature	Piezocapacitive/ thermoresistive	30-45	[9]
Pressure/temperature	Piezo-tribophotonic/ thermoresistive	30-50	[10]
Pressure/temperature	Reverse electrowetting/ thermogalvanic	5-31	[11]
Strain/temperature	Transmittance/ thermoresistive	25-42	[12]
Pressure/temperature	Piezoresistive/thermoresistive	25-50	[13]
Strain/temperature/pressure	Mechanochromic/thermoresistive /triboelectric	0-50	[14]
Pressure/temperature	Triboelectric	25-200	This work

Supplementary Table 2 | Comparison of the pressure sensitivity of P-TENG with reported triboelectric tactile sensors.

Multimodal sensing	Pressure range (kPa)	Sensitivity (V kPa^{-1})	Reference
PEDOT:PSS/eggshell membrane	0.25-250	2.4	[15]
PDMS/AgNW	0-150	1.187	[16]
Ecoflex/TPU	3-15	3.7	[17]
PDMS-PUa/PAA/bPEI	0-15;15-200	1.77;0.082	[18]
Liesegang-patterned ionic skin	0-35	1.5	[19]
FEP/CNF	0-8.36; 8.36-100	9.21;1.5	This work

Supplementary References

1. Niu S, Wang ZLJNE. Theoretical systems of triboelectric nanogenerators. **14**, 161-192 (2015).
2. Zhao J*, et al.* Remarkable merits of triboelectric nanogenerator than electromagnetic generator for harvesting small-amplitude mechanical energy. **61**, 111-118 (2019).
3. Lei H, Chen Y, Gao Z, Wen Z, Sun XJJoMCA. Advances in self-powered triboelectric pressure sensors. **9**, 20100-20130 (2021).
4. Wei X, Wang B, Wu Z, Wang ZLJAM. An open‐environment tactile sensing system: toward simple and efficient material identification. **34**, 2203073 (2022).
5. Tao J*, et al.* Self‐powered tactile sensor array systems based on the triboelectric effect. **29**, 1806379 (2019).
6. Xu C*, et al.* Raising the working temperature of a triboelectric nanogenerator by quenching down electron thermionic emission in contact‐electrification. *Adv Mater* **30**, 1803968 (2018).
7. Lin S*, et al.* Electron transfer in nanoscale contact electrification: effect of temperature in the metal–dielectric case. *Adv Mater* **31**, 1808197 (2019).
8. Shang C*, et al.* Soft Biomimetic Fiber-Optic Tactile Sensors Capable of Discriminating Temperature and Pressure. *ACS Appl Mater*, (2023).
9. An BW, Heo S, Ji S, Bien F, Park J-U. Transparent and flexible fingerprint sensor array with multiplexed detection of tactile pressure and skin temperature. *Nat Commun* **9**, 2458 (2018).
10. Ma X*, et al.* Bimodal tactile sensor without signal fusion for user-interactive applications. *ACS Nano* **16**, 2789-2797 (2022).
11. Liu K*, et al.* Self‐powered multimodal temperature and force sensor based‐on a liquid droplet. *Angew Chem Int Ed* **55**, 15864-15868 (2016).
12. Choi WY, Kwon JH, Kim YM, Moon HC. Multimodal Wearable Ionoskins Enabling Independent Recognition of External Stimuli Without Crosstalk. *Small*, 2301868 (2023).
13. Lee JH*, et al.* Rational design of all resistive multifunctional sensors with stimulus discriminability. *Adv Funct Mater* **32**, 2107570 (2022).
14. Zhang H*, et al.* Bioinspired Chromotropic Ionic Skin with In‐Plane Strain/Temperature/Pressure Multimodal Sensing and Ultrahigh Stimuli Discriminability. *Adv Funct Mater* **32**, 2208362 (2022).
15. Wei X*, et al.* A high-accuracy, real-time, intelligent material perception system with a machine-learning-motivated pressure-sensitive electronic skin. *Matter* **5**, 1481-1501 (2022).
16. Kang H*, et al.* Fingerprint‐inspired conducting hierarchical wrinkles for energy‐harvesting E‐skin. *Adv Funct Mater* **29**, 1903580 (2019).
17. Cui M, Guo H, Zhai W, Liu C, Shen C, Dai K. Template‐Assisted Electrospun Ordered Hierarchical Microhump Arrays‐Based Multifunctional Triboelectric Nanogenerator for Tactile Sensing and Animal Voice‐Emotion Identification. *Adv Funct Mater* **33**, 2301589 (2023).

18. Zhu M, Li J, Yu J, Li Z, Ding B. Superstable and intrinsically self‐healing fibrous membrane with bionic confined protective structure for breathable electronic skin. *Angew Chem Int Ed* **61**, e202200226 (2022).
19. Qiao H, Sun S, Wu P. Non‐equilibrium‐Growing Aesthetic Ionic Skin for Fingertip‐Like Strain‐Undisturbed Tactile Sensation and Texture Recognition. *Adv Mater*, 2300593 (2023).